

A Platform Integrating Acquisition, Reconstruction, Visualization, and Manipulator Control Modules for MRI-Guided Interventions

Jose D. Velazco Garcia 1 · Nikhil V. Navkar 2 · Dawei Gui 3 · Cristina M. Morales 1 · Eftychios G. Christoforou 4 · Alpay Ozcan 5 · Julien Abinahed 2 · Abdulla Al-Ansari 2 · Andrew Webb 6 · Ioannis Seimenis 7 · Nikolaos V. Tsekos 1

© Society for Imaging Informatics in Medicine 2018

Abstract

This work presents a platform that integrates a customized MRI data acquisition scheme with reconstruction and three-dimensional (3D) visualization modules along with a module for controlling an MRI-compatible robotic device to facilitate the performance of robot-assisted, MRI-guided interventional procedures. Using dynamically-acquired MRI data, the computational framework of the platform generates and updates a 3D model representing the area of the procedure (AoP). To image structures of interest in the AoP that do not reside inside the same or parallel slices, the MRI acquisition scheme was modified to collect a multi-slice set of intraoblique to each other slices; which are termed composing slices. Moreover, this approach interleaves the collection of the composing slices so the same k-space segments of all slices are collected during similar time instances. This time matching of the k-space segments results in spatial matching of the imaged objects in the individual composing slices. The composing slices were used to generate and update the 3D model of the AoP. The MRI acquisition scheme was evaluated with computer simulations and experimental studies. Computer simulations demonstrated that k-space segmentation and time-matched interleaved acquisition of these segments provide spatial matching of the structures imaged with composing slices. Experimental studies used the platform to image the maneuvering of an MRI-compatible manipulator that carried tubing filled with MRI contrast agent. In vivo experimental studies to image the abdomen and contrast enhanced heart on free-breathing subjects without cardiac triggering demonstrated spatial matching of imaged anatomies in the composing planes. The described interventional MRI framework could assist in performing real-time MRI-guided interventions.

 $\textbf{Keywords} \ \ MRI\text{-guided interventions} \cdot \ Dynamic \ three-dimensional \ reconstruction \ and \ visualization \ \cdot \ Oblique \ multi-slice \ imaging \cdot Control \ of \ MRI\text{-compatible robot}$

- Nikolaos V. Tsekos nvtsekos@central.uh.edu
- Department of Computer Science, University of Houston, Houston, TX, USA
- Department of Surgery, Hamad Medical Corporation, Doha, Qatar
- ³ GE Healthcare, Milwaukee, WI, USA

Published online: 27 November 2018

- Department of Electrical and Computer Engineering, University of Cyprus, Nicosia, Cyprus
- Department of Biomedical Device Technologies, Acıbadem Mehmet Ali Aydınlar University, Istanbul, Turkey
- ⁶ C.J. Gorter Center for High Field MRI, Leiden University Medical Center, Leiden, Netherlands
- Department of Medicine, Democritus University of Thrace, Alexandropoli, Greece

Introduction

The emergence of image-guided interventions with real-time MRI offers a unique range of benefits. Clinical procedures that may benefit from real-time, MRI guidance include interventions in the brain (electrode placement [1], laser ablation [2], and biopsy [3]), prostate (biopsy [4] and brachytherapy [5]), and breast (biopsy [6]). While conventional single-slice imaging may suffice for these procedures, multi-slice or three-dimensional (3D) intraoperative imaging in real-time may be needed for comprehensively imaging a larger dynamic Area of Procedure (AoP), such as intracardiac procedures on the beating heart [7, 8].

The collection of 3D real-time MRI data is challenging due to the low inherent sensitivity of the modality which therefore imposes a trade-off between speed and spatial coverage that can be achieved per frame. To address this, a typical approach is to collect a limited number of slices prescribed for imaging



specific anatomical landmarks or the interventional tools that are pertinent to the procedure [7, 9-15]. The collection of a limited number of appropriately prescribed slices is a fast and computationally efficient way for monitoring multiple aspects in the AoP. These slices, which we refer to as "composing slices," can be combined in the MR scanner coordinate system to generate dynamic 3D visualizations of the AoP during the intervention [11-13]. However, during such interventions, the position and shape of the anatomical structures within the AoP dynamically change due to physiological motion, voluntary or involuntary motion of the patient, as well as tissue dislocation caused by the procedure itself [13, 16]. Spatial mismatch of the "composing slices" may degrade 3D reconstruction of structures, potentially impacting the accuracy of the procedure and/or increasing the workload for the interventionist (who may need more time to inspect the 3D reconstruction). This situation may be exemplified when imaging a moving structure with sequential acquisition (i.e., one after the other) of multiple oblique slices in each time frame. When visualized on an interface for a given time instant, the 3D object will be depicted at different positions in the multiple slices obtained. Practically, this intraslice spatial mismatch is not noticeable when the composing slices are rendered two-dimensionally (2D) and viewed on individual windows on the graphical user interface [10, 17–19]. However, if the guidance is based on the 3D dynamic reconstructions, this mismatch becomes apparent on the 3D rendered view, the degree of which depends upon the speed of imaging and the motion of the structures [11, 12]. This previous work was motivated from the analysis of prior studies pertaining to the aforementioned spatial matching problem [11, 12] and the experience accumulated from performing robot-assisted phantom studies [13, 14, 20, 21] that highlighted two aspects: (i) in interventions, especially on moving organs, it is preferential to have spatial matching of the edges of critical structures (including anatomies and the interventional tool), and (ii) when robotic-assistance is used with real-time imaging, it is desirable to have at least the endeffector rendered, reconstructed, and visualized as a 3D object in the AoP along with the 2D images.

As an extension to previous studies, the aim of this work was to implement an integrated platform that will provide suitable tools for performing MRI-guided interventions to the clinician. Specifically, it introduces a computational pipeline of data and commands that links the MRI scanner, an interventional manipulator and the operator. The platform generates and updates a 3D model of the AoP based on a stream of MRI data. To address the situation when the AoP structures of interest do not reside on the same or parallel slices, we modified the imaging pulse sequence, and the corresponding computational framework, for the collection and visualization of intraoblique (i.e., oblique-to-each-other) composing slices. While interleaved acquisition of multiple slices, or groups of slices, is a standard commodity in modern clinical

MRI scanners, in this work, we implemented the acquisition of slices that are oblique to each other and that each one can be individually updated on-the-fly. With this scheme, same kspace lines of the different slices are collected at similar time windows for spatial matching of the imaged structures in the presence of motion. In addition, this work introduces further improvements upon two prior methodologies for performing robot-assisted and MRI-guided procedures by establishing the link between (i) on-the-fly multi-planar scanner control and MRI-based robot control [21] and (ii) preoperative planning and intraoperative imaging [20]. The interleaved k-space scanning approach implemented herein is initially studied with computer simulations to quantify the extent of the spatial mismatch in comparison to sequential scanning. The platform proposed and implemented is then evaluated experimentally for visualizing the motion of an MRI-compatible manipulator described previously [22] and for in vivo imaging of the heart and the abdomen. The clinical value of this work rests primarily on its potential to facilitate image-guided interventions, grounded in MRI-based visual-servoing of a robotic manipulator and its effective combination with an established imaging approach that was appropriately modified to provide 3D visualization of moving objects.

Materials and Methods

Computational Framework

The computational framework of the proposed platform for performing MRI-guided interventions is a data and command pipeline that integrates the MRI scanner, a robotic manipulator, and the operator. Figure 1 illustrates the architecture of the platform delineating its five primary modules and the flow of data and commands among them. This multi-threaded software was developed using C/C++ and software libraries (OpenGL for 3D rendering, Boost for network communication and multithreading, and FLTK for graphical user interface) tailored towards MRI-guided procedures [14, 15, 23]. The software runs on a dedicated workstation with task-specific parallel running threads for each module. If required, the computations of the reconstruction and visualization modules can be parallelized on a graphics processing unit (GPU) to speed up the reconstruction and 3D visualization (similar to [24]). The workstation interfaces with (i) the operator for providing visual cues about the procedure and receiving operator commands via a graphical user interface (GUI) and, optionally, a force-feedback interface (FFI) or joystick in the case that a robot is connected; (ii) the MRI scanner for (a) sending on-the-fly updated imaging parameter data and (b) receiving raw MRI data (i.e., before reconstruction), via local area network of the scanner, and, if used, (iii) an MR-compatible robotic device. To control the robot, the workstation sends control signals via an optical wire



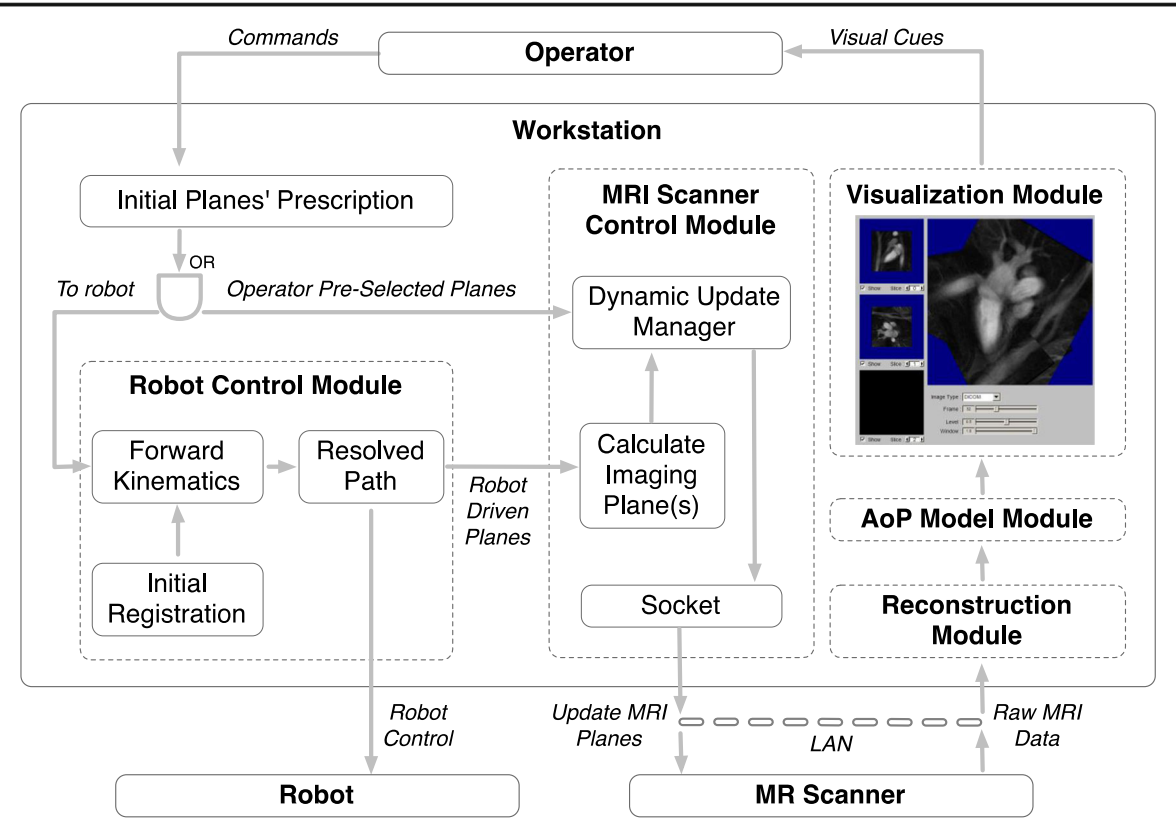


Fig. 1 Architecture of the implemented platform delineating the imaging, reconstruction, AoP modeling, and visualization modules, as well as the flow of data. The optional module for controlling an MR-compatible robotic device in MRI-guided interventions is also shown

that enters the MR scanner room via the waveguide. This architecture seamlessly integrates the operator, the scanner and, if used, a robot.

In its current implementation, this platform can support two modes of operation: (i) Mode A for manual manipulation of the interventional tool; in this mode, a priori prescription of the composing imaging planes and their dynamic on-the-fly update of the position and orientation is set manually by the operator using the GUI, and (ii) Mode B for robot-assisted manipulation of the interventional tool with robot-driven on-the-fly update of the imaging planes to follow the motion of the manipulator (as described in [21]). It is noted that, in the latter case, the operator still assigns the composing planes at the initial position of the robot (before initiation of its maneuvering) and the robot control module then adjusts these on-the-fly.

As shown in Fig. 1, two of the platform modules work together to image the AoP with the interleaved *k-space* acquisition of intraoblique slices (please refer to the following section for this MRI acquisition scheme). In Mode A, the input of the "MRI Scanner Control Module" is the imaging planes selected by the operator. In Mode B, the input is the robot kinematic posture (as calculated by the "Robot Control Module" secondary to a command of the operator) that is processed by a dedicated routine within the module that

calculates the set of planes needed to image an operator preselected part of the robot (i.e., the link(s), end-effector, interventional tool, etc.). This routine further converts the plane's position and orientation in the coordinate system format of the MRI scanner. In either case, the planes are then sent to the "Dynamic Update Manager" routine that transforms the corresponding information (i.e., plane position and orientation) into the file format of the particular MRI scanner (i.e., recognizable by the pulse sequence), supplied to a socket that then feeds them to another socket in the MRI scanner.

Interleaved Acquisition of the K-Space of Intraoblique Slices

The implemented data acquisition scheme interleaves the collection of the individual composing slices so that the same *k-space* lines (or segments of lines) of the composing slices are collected during adjunct time windows. It is based on the hypothesis that such time-matching of the same *k-space* lines of all composing slices will minimize the spatial mismatch of the depicted structures. These intraoblique composing slices are then reconstructed in 3D space as they are collected. In this context, the proposed approach is a multi-slice, intraoblique alternative to 3D MRI for performing dynamic volumetric imaging of an AoP.



Figure 2 illustrates the data collection, reconstruction, and visualization processes of imaging the AoP with the proposed approach. As depicted in Fig. 2a, the sequence loops first over the time frames (index k), then the slices (index m), and then over the same segments or individual *k-space* lines of the composing slices (index j). The arrow shows the preferential positions for placing an optional cardiac triggering signal. As a result, the same *k-space* lines or segments of *k-space* lines are collected during similar time instances along the timeline of the object motion and, thus, temporospatial matching of the imaged structures is provided.

After collecting a frame, i.e., a complete set of k-space segments or lines of all composing slices, the raw data are pushed via the Ethernet connection to the workstation and fed to the "Reconstruction Module." As illustrated in Fig. 2c, the segments or individual k-space lines are ordered per slice, fill in the k-space matrix of the corresponding composing slice, and are fast Fourier transformed (FFT) to generate the images (i.e., spatial domain). The module reconstructs the composing planes based on the current header information and, therefore, if any of the aforementioned parameters is changed interactively (from the operator in Mode A or the robot in Mode B), this is reflected in the current refreshing cycle of the 3D scene (Fig. 2d). The composing slices are then fed to the "AoP Model Module" that refreshes the corresponding slices in the 3D AoP scene by replacing them in 3D space relative to the coordinate system of the MRI scanner. The "Visualization Module" continuously updates the GUI with newly reconstructed data in the form of 3D composing slices (Fig. 2e) as well as with the individual slices (Fig. 2f).

The operation of this acquisition scheme can be appreciated by considering a continuous linear translation in real space, which results in a phase shift in the *k-space* [25]. The larger the difference in the spatial position of the object when each

composing slice is collected, the larger the phase shift induced by this motion. Specifically, each point (n) of every k-space line (j) of each plane (m) is modulated by a phase shift $(\Delta \emptyset_R)$ which depends on the speed of motion (u_R) , and the exact instance at which it was collected $(t_m(n,j))$, i.e.,

$$\Delta \varnothing_{\rm R} = 2\pi k_{\rm PHASE} u_{\rm R} t_{\rm m}(n, j).$$

Considering the interleaved acquisition in Fig. 2a, for the same *k-space* line of two composing slices, their phase shift difference is

$$\Delta \varnothing_{\mathrm{R}} = 2\pi \mathrm{k}_{\mathrm{PHASE}} u_{\mathrm{R}} [t_{\mathrm{m}}(n,j) - t_{\mathrm{m+1}}(n,j)]$$

$$= 2\pi \mathrm{k}_{\mathrm{PHASE}} u_{\mathrm{R}} \cdot \frac{N_{\mathrm{MATRIX}}}{N_{\mathrm{SEGM}}} . TR$$

where $N_{\rm MATRIX}$ is the acquisition matrix and $N_{\rm SEGM}$ is the number of k-space segments. Minimizing the phase shift in the k-space would result in better spatial matching of the composing slices and, thus, more accurate representation of the imaged structures. The motion induced phase difference becomes smaller when the number of segments ($N_{\rm SEGM}$) is increased. Its minimum value $2\pi k_{\rm PHASE} u_{\rm R}$. TR is attained with $N_{\rm MATRIX} = N_{\rm SEGM}$.

Simulation Studies

Simulations were performed with in-house developed software in MATLAB (Mathworks, Natick, MA) to assess the effects of segmentation and motion on a 3D reconstructed virtual object using two composing planes. The simulated object was a virtual box ($128 \times 128 \times 32$ pixels) subjected to linear motion with constant speed along the axis perpendicular to its largest surface. The virtual box moved inside a 3D volume ($128 \times 128 \times 128$

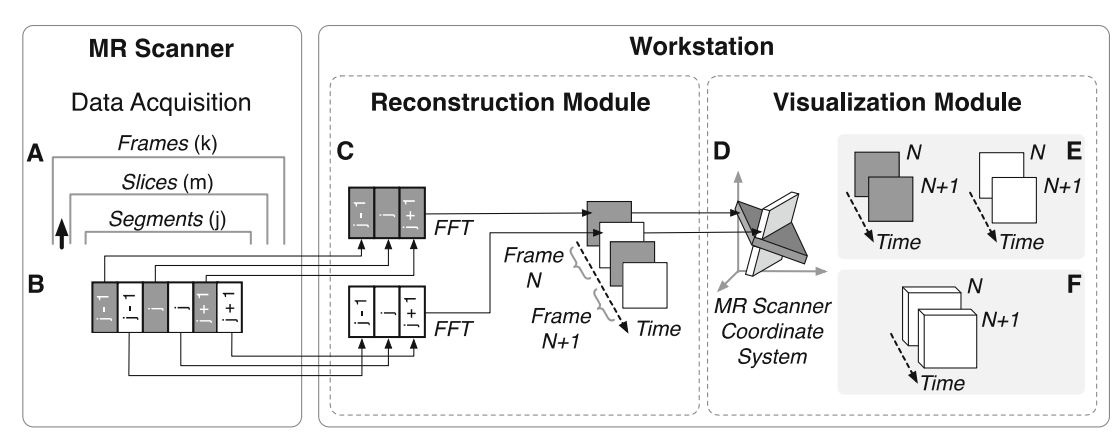


Fig. 2 The imaging, reconstruction, and visualization components of the proposed platform. **a** The structure of the pulse sequence loops for dynamic imaging. The black arrow shows the preferential position of optional triggering signal. **b** Diagram of the general principal of interleaving the acquisition of the same segments of different oblique to each other composing slices, so the same segments of these slices are collected at similar time instances. **c** Diagram of the process performed

at the reconstruction module illustrating a two-composing slice set. After segment ordering, the complete k-space of the composing slices is fast Fourier transformed (FFT) generating the corresponding images of the multi-slice set on their oblique coordinate systems. \mathbf{d} The visualization module places the composing slices on the coordinate system of the scanner in a 3D volume. The individual slices (\mathbf{e}) and their 3D reconstruction (\mathbf{f}) are then refreshed on a user interface



128 pixels) that represents the imaging field-of-view (FOV). The views of the object in the composing slices were generated starting with an initial position at the center of the FOV. The read-out axes of the two composing slices were placed parallel to the motion (white arrow in Fig. 2a), since this choice results in fewer artifacts compared to the motion parallel to the phase encoding axis, and is often used in practice. Linear constant speed motion was evaluated as previously described [25]. The sampled transverse magnetization, $M_{\rm XY,SLm}^{(J)}$, for the $J^{\rm th}$ k-space line of slice m (m = 1 and 2) was calculated analytically. As an example, for slice m = 1:

$$\begin{split} M_{\mathrm{XY,SL1}}(^{\mathrm{J})} &= |\mathrm{sin}(\alpha).M_{\mathrm{Z,SL1}}(^{\mathrm{J})}| = |\mathrm{sin}(\alpha).\\ &\left[M_{\mathrm{Z,SL1}}{}^{\infty} + \left(M_{\mathrm{Z,SL1}}(^{\mathrm{J-1})}.\mathrm{cos}(\alpha) - M_{\mathrm{Z,SL1}}{}^{\infty} \right).\mathrm{e}^{\frac{-T_{REP}}{T1}} \right]| \end{split}$$

where M_Z is the longitudinal magnetization, α is the excitation angle and the repetition time $T_{\rm REP} = TR$ (within the segment of the same slice 1) or $T_{\rm REP} = (N_{\rm MATRIX}/N_{\rm SEGM}).TR$ (during the acquisition of the other slice). Acquisition parameters were as follows: matrix size $N_{\rm MATRIX} = 128 \times 128$, TI = 800 ms, excitation angle $\alpha = 20^{\circ}$, and TR = 2 ms. The simulations evaluated different speeds, up to 125 mm/s (corresponding to the fastest average speed of cardiac motion [26]), and segmentation schemes. The output of the simulation were the views of the object in the two orthogonal composing slices (SL1 and SL2), a 3D reconstruction of the two planes in the coordinate system of the object, the signal intensity (SI) profiles along each plane, and the longitudinal magnetization of each k-space line before and after an excitation pulse (reported relative to time).

Robot Visualization MRI Studies

The implemented platform was evaluated with phantom studies to observe in 3D the maneuvering of an MRI-compatible manipulator with tubing (filled with water and 3% gadolinium-based contrast agent) attached to its end-effector [21, 22]. Slices were prescribed to image different parts of the manipulator and were changed on-the-fly to follow the motion of a particular link of the device via the manipulator-driven MRI described before [21]. Imaging was conducted on a 1.5 T MR scanner (Siemens Healthcare, Erlangen, Germany) with a short repetition (TR) and echo (TE) time gradient recalled echo (GRE) pulse sequence ($TR/TE/\alpha = 3.97 \text{ ms}/1.74 \text{ ms}/40^\circ$, slice thickness = 8 mm, acquisition matrix size = 192X192, $FOV = 260 \times 260 \text{ mm}^2$).

In Vivo MRI Studies

Pilot in vivo studies were performed on healthy volunteers with informed consent obtained from all subjects under a protocol approved by the review boards. The studies assessed the

described interleaved acquisition to image (i) the abdomen (n=2) and (ii) for contrast-enhanced cardiac imaging (n=1)1). All studies were performed on a 1.5 Tesla scanner (Siemens Healthcare) using the body coil for transmission and a 12-channel abdominal phased array coil (six anterior and six posterior elements) for signal reception. In these studies, we used linear k-space line ordering (i.e., most negative to most positive). In the abdominal study, the subjects were instructed to breathe freely and imaging was performed without any respiratory gating. Three intraoblique slices were prescribed through the abdomen of the volunteer and continuous acquisition of multiple frames was performed with a spoiled gradient recalled echo $(TR/TE/\alpha = 3.97 \text{ ms}/1.74 \text{ ms}/40^\circ)$, $FOV = 295 \times 295 \text{ mm}^2$, and slice thickness = 10 mm) using $N_{\text{SEGM}} = 96$ for a matrix size = 192×192 (i.e., N_{SEGM} / $N_{\rm MATRIX} = 1/2$). In the cardiac study, the interleaved acquisition was used to image the heart and the great vessels during the passage of Gd-based contrast agent using a saturation recovery (SR) prepared spoiled gradient recalled echo sequence with parameters $TR/TE/T1/\alpha = 2.45 \text{ ms}/1.3 \text{ ms}/5 \text{ ms}/40^{\circ}$, ma $trix = 96 \times 128$, $FOV = 200 \times 200 \text{ mm}^2$, and slice thickness = 10 mm. Interleaving segmentation was implemented with $N_{\rm SEGM}$ = 48. Two intraoblique slices were then prescribed and repetitive acquisition was commenced; after five baseline frames the subject was administered with Gadoliniumbased contrast agent (volume = 10 ml each and 2 ml/s infusion rate). The individual frames were then reordered and reconstructed in 3D.

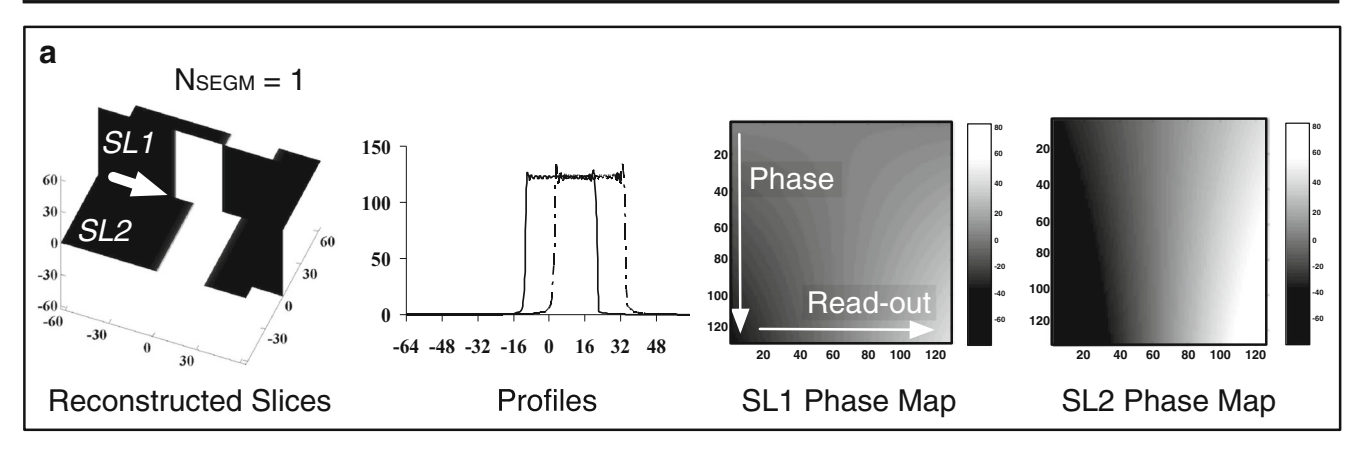
Results

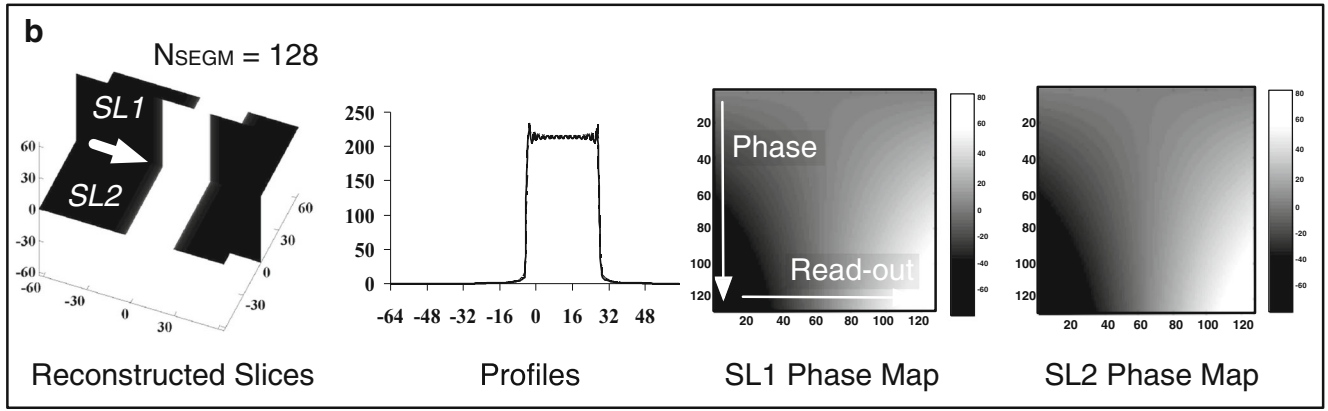
Simulation Studies

Figure 3 reviews representative results from the simulations regarding the moving virtual object imaged with the two composing slices SL1 and SL2. Figure 3a and b compare the two extreme cases of no segmentation ($N_{\rm SEGM}=1$) and maximum segmentation ($N_{\rm SEGM}=N_{\rm MATRIX}=128$) of k-space. With the essentially sequential acquisition of the composing planes presented in Fig. 3a the slices are collected at time windows differing by $N_{\rm MATRIX}.TR$ (i.e., 256 ms), which results in a spatial mismatch of the two views of the object. This manifested in both the edges of the 3D reconstructed slices and the profile graphs. The effect of sequential acquisition is also reflected in the phase maps of the two slices which demonstrate that translation in the spatial domain results in phase shifts in k-space [25] by:

$$\Delta \varnothing_{\rm R} = 2\pi k_{\rm PHASE} \cdot \frac{N_{\rm MATRIX}}{N_{\rm SEGM}} \cdot \frac{u_{\rm R}}{FOV} \cdot TR.$$







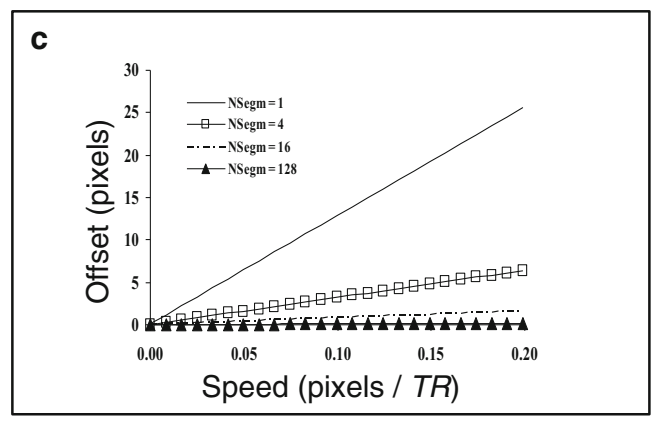
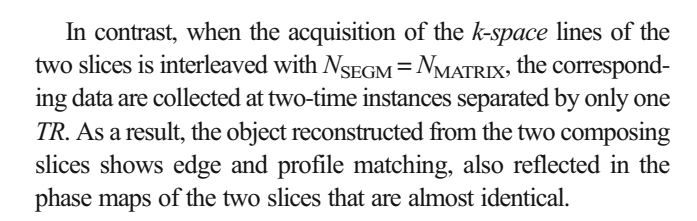
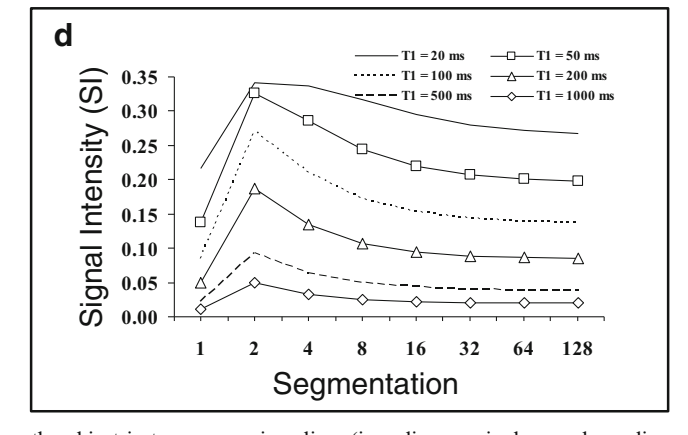


Fig. 3 Representative results from simulations. **a** and **b** reconstructed slices of the two composing slices (orthogonal planes), the corresponding profiles of the object, and the phase maps of the two slices when the virtual object moves with a speed of 50 mm/s (0.10 pixels/TR) with number of segmentations $N_{\rm SEGM} = 1$ (**a**) and $N_{\rm SEGM} = 128$ (**b**). Simulation parameters were $N_{\rm MATRIX} = 128 \times 128$, excitation angle = 20°, ten steady state frames, pixel size of 1 mm, and a TR (repetition time) of 2 ms. **c** The difference (offset) between the center of





the object in two composing slices (i.e., slice acquired second vs. slice acquired first) for $N_{\rm SEGM}=1$, 4, 16, 128 (matrix size = 128). This offset corresponds to the mismatch between the views of the object on the two composing slices. The speed is in pixels per TR and, for a TR=2 ms and voxel size 1 mm, corresponds to 100 mm/s. **d** The dependence of the collected signal to the number of segments for different TI (longitudinal relaxation time) values (the number of segments are equally distributed to show the dependence at low $N_{\rm SEGM}$)

The graph in Fig. 3c demonstrates the effect of object speed and acquisition segmentation on the spatial mismatch of the object center as depicted in the two composing slices. As expected, the peak-to-peak difference of the two views increases with increased speed and reduced segmentation. Interleaving and segmenting the acquisition modulates the



 M_Z and thus the acquired signal. As illustrated in Fig. 3d, for any $N_{\rm SEGM} > 1$ the M_Z and SI are higher than those with $N_{\rm SEGM} = 1$ for all TI values simulated, since interleaved acquisition increases the M_Z recovery time between segments. Also, increased segmentation reduces the SI since there is less time for longitudinal recovery between segments. As expected, the lower the T1, the higher the signal intensity.

Robot Visualization MRI Studies

Results from using the interleaved acquisition technique to image and visualize the motion of an MR-compatible robotic manipulator are presented in Figs. 4 and 5. Details of the robotic manipulator (Fig. 4a) are described in our previous work [21, 22]. In these studies, we investigated the method with the manipulator-driven MRI approach [21] incorporated into the computational core of the system, as shown in Fig. 1. In the case shown in Fig. 4, two intraoblique imaging planes (Fig. 4b–d) were prescribed to image two of the distal links of the manipulator. With the manipulator-driven MRI activated, the planes were changed on-the-fly to include the marker tubes as the

manipulator was maneuvered. The two slices were then segmented and the marker tubes were rendered in 3D in the reconstruction module of the computational core (Fig. 4e and f). In these figures, the 3D frames were superimposed to show the actuation of the corresponding degree-of-freedom. In all cases, the interleaved acquisition resulted in the accurate rendering of the marker tubes from the composing planes without any spatial mismatch due to the motion of the manipulator (at speeds of 0.05 to 0.10 pixels per TR). These figures also show an artefactual signal generated from the ultrasonic motors that were not sufficiently shielded in these studies. Another example of spatial matching between the composing slices of the moving manipulator is illustrated in Fig. 5. In this case, three planes (Fig. 5a-c) were used to track the motion of the end-effector with the manipulatordriven MRI activated to track the gadolinium-filled introducer sheath (Fig. 5a) and a 2D cross-shaped marker (Fig. 5c). Figure 5d shows the interleaved acquisition to accurately reconstruct the marker without any mismatch despite the continuous motion of the manipulator with a speed of 0.08 pixels per TR.

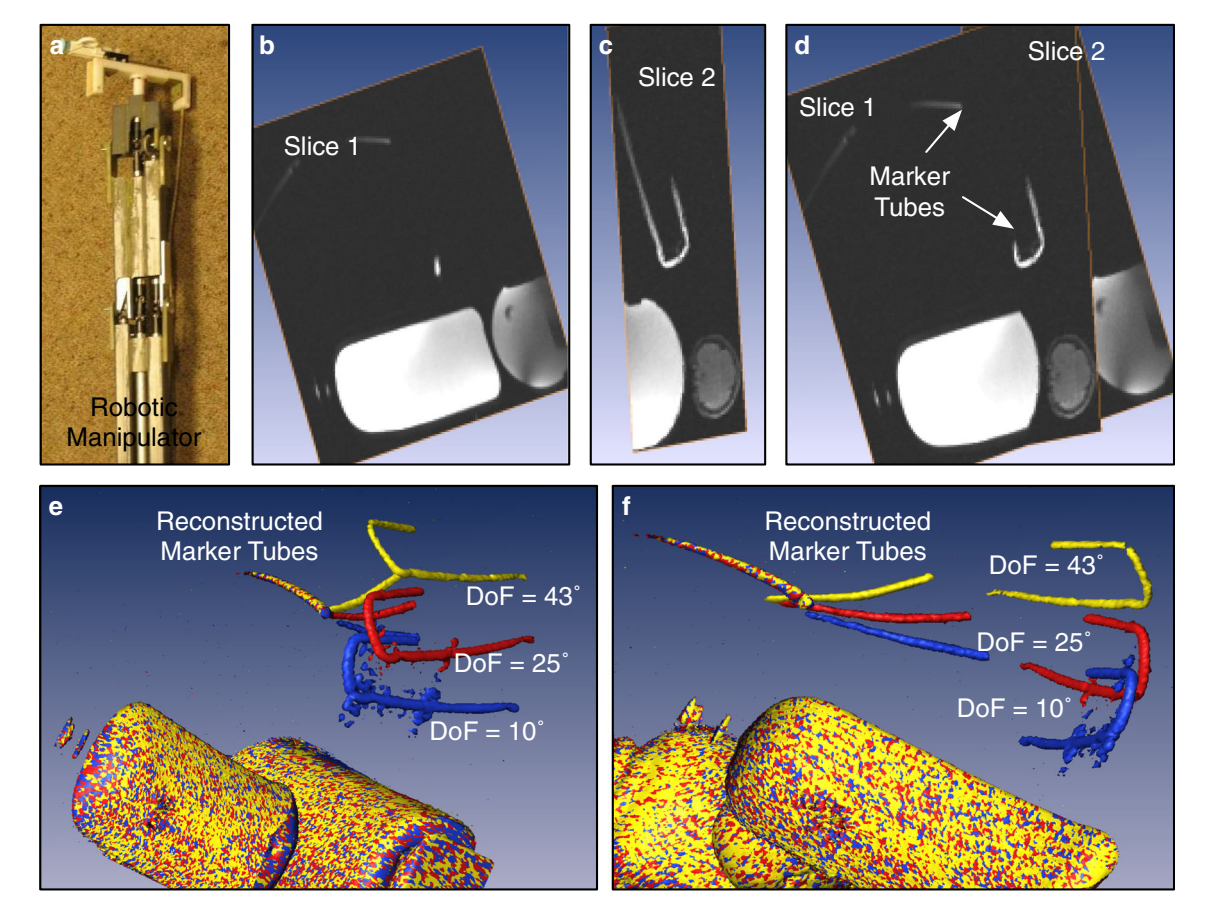
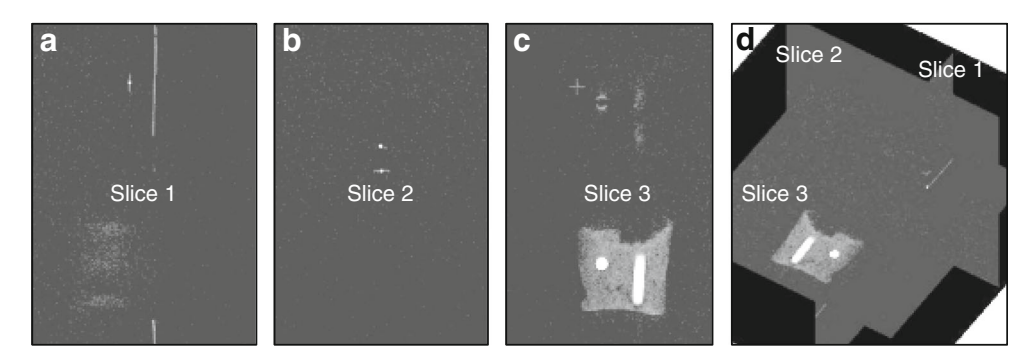


Fig. 4 Representative results from monitoring the maneuvering of an MR-compatible robotic manipulator (**a**) with two high spatial resolution $(1.1 \times 1.1 \text{ mm}^2)$ composing slices (**b**) and (**c**). The slices' orientation is updated on-the-fly to image the links of the manipulator (**d**), via the

manipulator-driven approach. The visualization module generates (e) and updates (f) a virtual reality scene that shows the accurate reconstruction of the manipulator during motion



Fig. 5 Visualization of the maneuvering of an MR-compatible manipulator on the three composing planes (a, b, and c), as well as their 3D reconstruction on-the-fly (as the manipulator maneuvers) (D)



In Vivo MRI Studies

Figure 6 shows representative results of imaging the human abdomen during free-breathing using three intraoblique

composing planes (Fig. 6a–c). The slice intersections are delineated as hypo-intense bands, compared to the rest of the image, since they experience excitation pulses during the acquisition of both intersecting slices. The composing

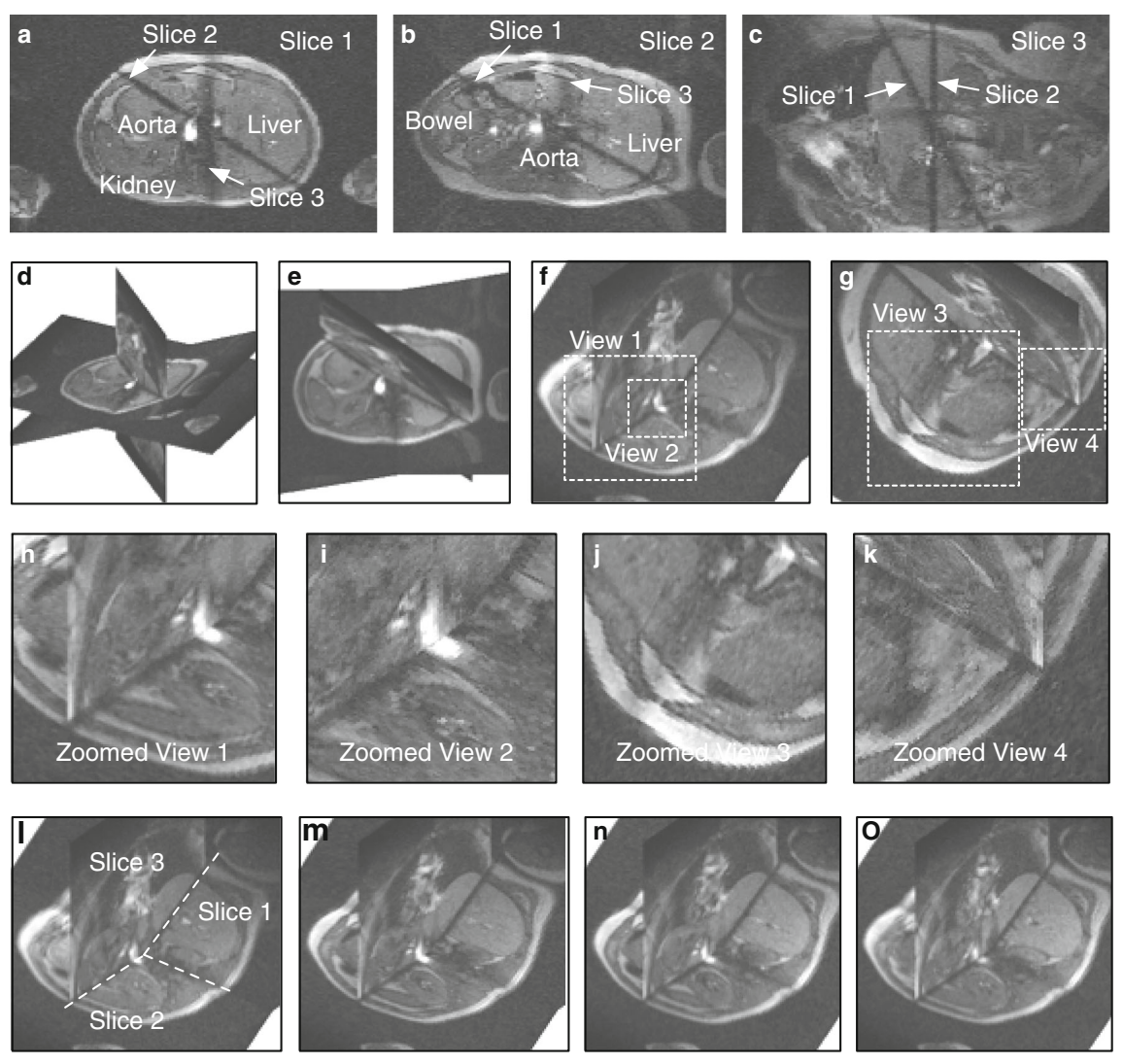


Fig. 6 Representative results from an interleaved k-space acquisition of three composing slices (a, b, and c) while the subject was breathing freely. The arrows identify the intercept of the slices. Different views (d, e, f, and g) of the three planes reconstructed in the scanner coordinate system on the visualization interface. The dashed boxes in f and g delineate the four

areas of the 3D reconstruction shown in zoomed view (**h**, **i**, **j**, and **k**). These frames were collected with interleaving segmentation of $N_{\rm SEGM}$ = 96 for a matrix size 192 × 192. Four consecutive time frames (**l**, **m**, **n**, and **o**) of the 3D reconstructed composing planes (intersecting along the dashed white lines in **l**)



slices were reconstructed in the 3D space defined by the MRI scanner's coordinate frame after extracting the exact coordinates from raw data headers. The resulting 3D volume was then available for on-the-fly manipulations such as 3D rotations (Fig. 6d-g) and zooming (Fig. 6h-k) that can be integrated into an interventional procedure [17, 18, 22]. Figure 6h-k also show spatial details from the 3D reconstructed composing slices and demonstrate the matching of the edges of the different anatomical structures attained with interleaved acquisition. Additionally, Fig. 61-o present a series of four consecutive time frames generated from the dynamically updated, 3D reconstructed composing planes. The hypo-intense bands that correspond to the intersections of the slices are also evident. Since the intersection bands receive continuous pulsing in every TR, their longitudinal magnetization ($M_{Z,INTBAND}$) is brought to, and maintained at a steady state. In the case that the composing planes are collected with the same TR, independent of the acquisition segmentation, $M_{Z,INTBAND}$ is given by:

$$M_{\rm Z,INTBAND} = M_{\rm Z} \propto \frac{1 - e^{\frac{-TR}{T1}}}{1 - \cos(\alpha)e^{\frac{-TR}{T1}}}$$

Figure 7 illustrates results from a two-composing slice imaging and reconstruction implementation of the great vessels and heart during the passage of gadolinium-based contrast agent acquired with $N_{\rm SEGM} = 48$ and a 96×128 matrix size (during a breath-hold and with cardiac triggering). The images in Fig. 7a–d show the two composing slices, before the initiation of infusion (Fig. 7a and c) and during the passage (Fig. 7b and d) of the contrast agent. Notably, and in contrast to the results presented in Fig. 6, the intersection of the two slices is not observed: in the absence of contrast agent, the inversion recovery sequence nulls the myocardial signal, while during the passage of the agent, the short TI of the blood in the vessels and the cardiac cavities results in sufficient recovery of the intersection bands. Different views of the 3D reconstructed composing slices are shown in Fig. 7e and g.

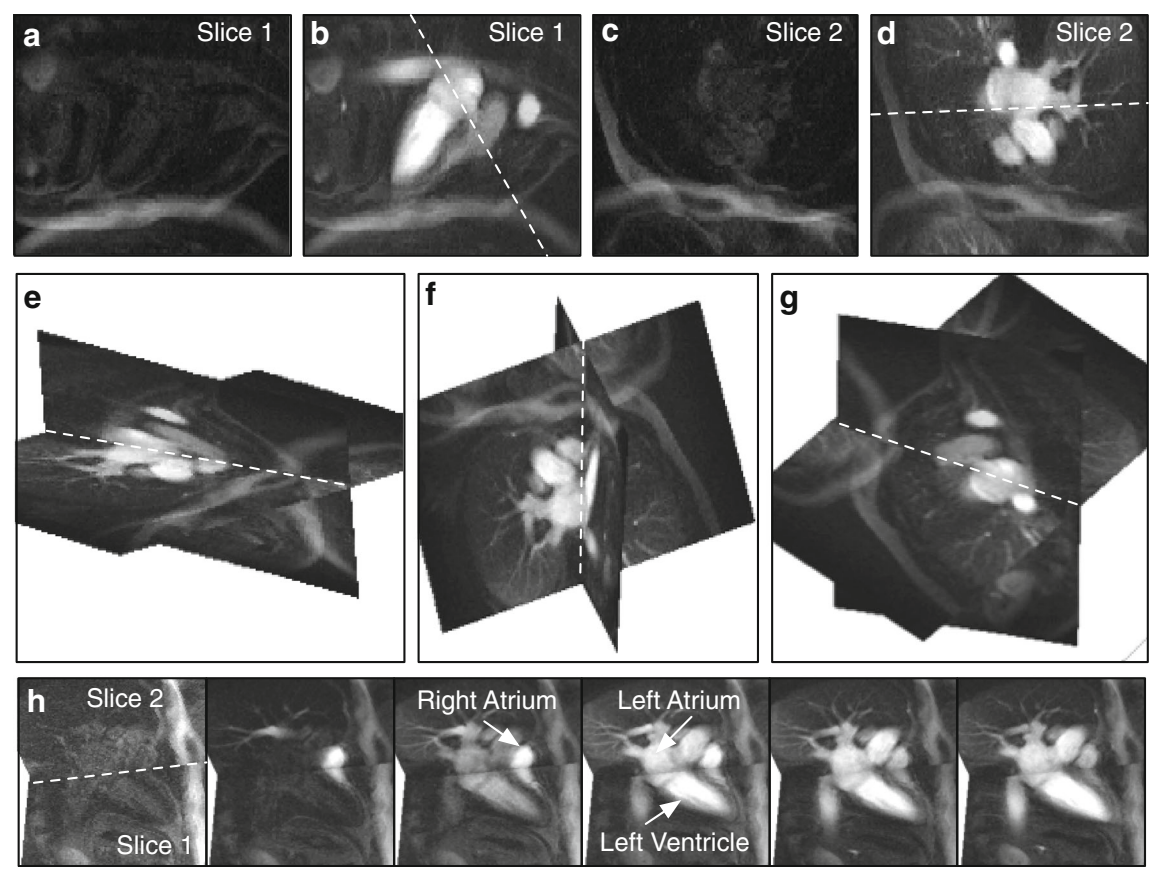


Fig. 7 Representative results from a bi-planar interleaved k-space imaging and reconstruction scheme of the human heart during peripheral IV-infusion of gadolinium-based contrast agent (**a** to **d**): the two composing slices, before (**a** and **c**) and during (**b** and **d**) the passage of the contrast agent. The dashed lines identify the intercept of the slices. A panel of three different 3D reconstructed views of the two composing

slices (**e**, **f**, and **g**) generated on the visualization interface. A series of time frames (**h**) depicting the passage of the contrast agent through the heart and great vessels in the 3D reconstructed composing planes. These frames were collected with interleaving segmentation of $N_{\rm SEGM}$ = 48 for a matrix size 96×128



The panel of images in Fig. 7h shows a series of six-time frames of 3D reconstructions at selected instances before (first frame) and during—the passage of the agent. The contrast agent passage can be appreciated from the contrast enhancement of the different blood pools. Since the frames in panel Fig. 7h were collected during breath-holding and with cardiac triggering, the heart appears "frozen" in the same diastolic phase of the cardiac cycle.

Discussion

An important feature for performing complex minimally invasive procedures under MRI guidance is the ability of MRI to dynamically collect 2D, multi-slice, or 3D data sets in any prescribed orientation. This property is further enhanced when the imaging plane orientation is interactively changed on-thefly to depict the interventional tool as it is maneuvered through the body [10, 21, 27]. During a procedure, the spatial position and shape of the anatomical structures of interest may change dynamically due to a variety of reasons, including physiological respiratory and/or cardiac motion, voluntary or involuntary motion of the patient, tissue dislocation secondary to the advancement of the interventional tools, or swelling or hemorrhage. Moreover, a procedure may require visualization of MRI-compatible actuated manipulators which articulate or bend in 3D space [28]. With updated volumetric imaging, such changes can be visually tracked as they occur, allowing for appropriate interventions. Also, as has been suggested before [11, 29], visualizing the procedure in a single window, rather than viewing two or more planes in individual windows, can be more efficient since the clinician performing intervention would not need to scan through multiple windows. As has been demonstrated before, a general solution to the rather slow refresh rate of real-time MRI is the continuous collection of a limited number of slices that are prescribed to track objects of interest; often these slices are intraoblique ([7, 11, 13–15, 30, 31] and references therein).

When a moving object of interest is imaged with two or more intersecting slices which are used as composing planes for 3D reconstruction, the sequential acquisition of these slices results in spatial mismatch of the 3D reconstructed structure. This mismatch is more pronounced in MRI-guided cardiac procedures [7, 11–13, 32]. For addressing such spatial mismatches, Navkar et al. [33] proposed virtual fixture techniques from three sequentially collected intersecting slices to generate a mesh along the tissue boundary. The described technique was implemented for interventional studies that were performed under real-time, MRI-guidance and required visualization of different moving objects of interest in the AoP with more than one slice. In the current work, the intraoblique composing slices are time matched by interleaving the acquisition of the same segments or individual lines of the *k-space*

from all slices (Fig. 2). Temporospatial matching is based on collecting the same k-space lines of all composing slices at similar time points. This occurs especially when $N_{\rm SEGM}$ = N_{MATRIX} , i.e., when the same k-space line for all composing planes is acquired with a time separation of one TR. This acquisition pattern results in almost identical phase modulation of the different slices (Fig. 3). As shown with manipulator tracking (Figs. 4 and 5) and in vivo (Figs. 6 and 7) MRI studies, the composing planes consistently depict the different object's views at spatially matched positions. Time matching of the slice acquisition, in each frame, results in spatial matching of the structures and anatomical features depicted in the composing slices. Interleaved acquisition of slices is a well-established data collection strategy in MRI, primarily used to optimize data acquisition in long TR sequences, including the traditional Spin Echo (SE) and the T1weighted-Fluid-Attenuated Inversion Recovery (T1-FLAIR) sequences. In this work, the interleaved acquisition strategy was modified. The main difference in the proposed implementation lies in the insertion of alternating slice profiles for the different slices such that slices are not simply stacked. As expected, line shift errors are avoided with the implemented k-space ordering.

The employed multi-slice acquisition scheme which acquires slices oblique to one another could potentially suffer from specific artifacts. First, eddy currents may dynamically influence both the local main field and applied magnetic field gradient, particularly those generated by the ramp-up and ramp-down portions of the trapezoidal gradients used in the spoiled gradient echo sequence. In modern clinical scanners, however, the major components of eddy currents are compensated for several different time constants. Under these conditions, the effect of any residual eddy currents is considered to be rather small and is expected to have negligible influence on gradient linearity and spatial accuracy. A second potential source of errors can be orientation-dependent concomitant gradients, i.e., small non-linear magnetic field gradient components present in the direction transverse to the applied direction [34]. It is well-known that these components can induce phase errors in the reconstructed image. Their effects include blurring in k-space, producing a parabolic phase variation across the imaging plane, and shifting k-space data in the frequency domain due to a linear phase component. Typically, concomitant gradients are only significant when very strong gradients are used at a very low static field strength, which is not the situation here. Any small linear phase ramp would also not be detrimental to our study, since it uses only magnitude-based images.

As reported before in neurosurgical applications [16, 35, 36], when a limited number of slices is required, the acquisition planes most often are non-parallel. In such interventions, dynamic generation of cut-through views from dual oblique plane acquisitions would suffice for real-time imaging to



guide the procedure. The interleaved technique implemented herein can be used to generate dynamically updated cutthrough sections of the AoP (as shown in Figs. 6 and 7). Coupled with the technical capability of modern commercial MRI scanners for on-the-fly adjustments of the imaged planes directly from a computer-controlled manipulator [21], the technique offers the capability to visualize articulated or bendable tools with a small number of slices (such as shown in Figs. 4 and 5).

The described interleaved acquisition scheme modulates the SI of the collected composing planes. First, as for any other sequence that collects interleaved non-parallel slices, it demonstrates low SI bands at their intersections. The width of these bands depends on the bandwidth and profile of the excitation pulse, as well as on the relative angle of the intersecting slices. Unless an intersection corresponds to anatomical aspects of interest, practically these bands will not affect the visual perception and utility of the 3D reconstruction. Also, when a gadolinium-based contrast agent is used, the fast-longitudinal relaxation of the enhanced structures reduces or eliminates these bands, as shown in Fig. 7. With the interleaved acquisition scheme, additional SI modulation originates from the competing effects of segmentation and interleaving (Fig. 3d). Specifically, smaller N_{SEGM} values increase the frequency of RF pulsing for a given slice and thus reduce its magnetization, whereas interleaving increases longitudinal relaxation signal recovery between the segments (Fig. 3c and d). As shown in Fig. 3, the case of $N_{\text{SEGM}} = N_{\text{MATRIX}}$ provides the best possible temporospatial matching along with moderate loss of signal. Notably, for any ratio $N_{\rm MATRIX}/N_{\rm SEGM}$, the SI is higher compared to sequential non-segmented acquisition, since the sustained excitation pulses of the latter reduce the M_Z of the same slice (Fig. 3d).

While slice-interleaved acquisition offers spatial matching of moving objects imaged by multiple slices, its practical merit depends on the particular needs of a procedure, i.e., if high spatial accuracy in rendering structures is needed. Moreover, a potential drawback of the method is that the actual TR (i.e., the repetition time of an individual k-space line or k-space segment of a certain slice) increases compared to when individual slices are collected sequentially. However, simulating for the linear motion of an object with a velocity of up to 125 mm/s (Fig. 3), as well as non-triggered cardiac imaging (Fig. 7), demonstrated that interleaved acquisition with a high N_{MATRIX}/N_{SEGM} ratio shows excellent spatial matching and no motion artifacts. Nevertheless, one should be aware of this potential limitation, which also affects image contrast, and if it is encountered then the $N_{\rm MATRIX}/N_{\rm SEGM}$ ratio should be adjusted. The interleaved scheme proposed lengthens the total acquisition time and this may lead to image blurring due to gross motion. Acquired data, however, suggest that the degree of blurring does not impact considerably edge matching in 3D rendering.

Several aspects of this work require further investigation. First, while the simulations demonstrated the impact of motion and segmentation on the spatial matching and SI, they were limited to a continuous linear motion. More detailed assessment of the slice-interleaving, especially for cardiac imaging, would require simulating more realistic speed/ displacement waveforms [37]. This is a future direction for expanding the simulation software for including such waveforms, as well as incorporating triggering and selective acquisition of the segments as described previously [38]. The second focus area will be the implementation of the technique for visualizing the entire length of bendable structures (e.g., snake-like manipulators) that maneuver in 3D and do not reside in a single plane. For high-definition visual effects and further acceleration, the third area entails the implementation of image reconstruction and visualization rendering pipeline on a GPU [24], as well as the incorporation of a holographic interface for improved visualization and planning [39]. After implementing such improvements, we plan to pursue user studies to fully assess this platform with in vivo experiments.

Conclusions

Dynamic imaging of an area of interest with a limited number of intraoblique composing slices, acquired and reconstructed in 3D in such a way that reflects anatomical matching of the structures, can satisfy the needs for real-time guidance of interventional procedures. The described platform, which comprises of an interleaved and segmented acquisition scheme of intraoblique slices, the 3D reconstruction of spatially matched structures in the composing planes, an appropriate visualization tool, as well as a robot control module, provides dynamic volumetric imaging of moving objects. The technical novelty of this work rests primarily on its robotic component, while its clinical value lies mainly in the potential of the integrated platform to facilitate image-guided interventional procedures with MRI-based visual-servoing of a robotic manipulator. Future directions should include comprehensive simulations to assess more realistic motion waveforms and the implementation of this k-space scanning approach using faster pulse sequences for imaging of snake-like manipulators.

Acknowledgements This work was supported in part by the National Science Foundation grant CNS-1646566, a Greek Diaspora Fellowship granted by the Stavros Niarchos Foundation and administered by the Institute of International Education, as well as the Qatar National Research Fund award NPRP9-300-2-132 by Qatar Foundation.

Disclaimer All opinions, findings, conclusions, or recommendations expressed in this work are those of the authors and do not necessarily reflect the views of our sponsors.



References

- Martin AJ, Larson PS, Ostrem JL, Keith Sootsman W, Talke P, Weber OM, Levesque N, Myers J, Starr PA: Placement of deep brain stimulator electrodes using real-time high-field interventional magnetic resonance imaging. Magn Reson Med 54(5): 1107–1114, 2005
- Jolesz FA: Future perspectives for intraoperative MRI. Neurosurg Clin N Am 16(1):201–213, 2005
- Scheer JK, Hamelin T, Chang L, Lemkuil B, Carter BS, Chen CC: Real-time magnetic resonance imaging-guided biopsy using SmartFrame® Stereotaxis in the setting of a conventional diagnostic magnetic resonance imaging suite. Oper Neurosurg (Hagerstown) 13(3):329–337, 2017
- Giganti F, Moore CM: A critical comparison of techniques for MRI-targeted biopsy of the prostate. Transl Androl Urol 6(3): 432–443, 2017
- Borot de Battisti M, Denis de Senneville B, Hautvast G, Binnekamp D, Lagendijk JJW, Maenhout M, Moerland MA: A novel adaptive needle insertion sequencing for robotic, single needle MR-guided high-dose-rate prostate brachytherapy. Phys Med Biol 62(10):4031–4045, 2017
- Liberman L, Bracero N, Morris E, Thornton C, Dershaw DD: MRIguided 9-gauge vacuum-assisted breast biopsy: initial clinical experience. AJR Am J Roentgenol 185(1):183–193, 2005
- McVeigh ER, Guttman MA, Lederman RJ, Li M, Kocaturk O, Hunt T, Kozlov S, Horvath KA: Real-time interactive MRI-guided cardiac surgery: aortic valve replacement using a direct apical approach. Magn Reson Med 56(5):958–964, 2006
- Saikus CE, Lederman RJ: Interventional cardiovascular magnetic resonance imaging: a new opportunity for image-guided interventions. JACC Cardiovasc Imaging 2(11):1321–1331, 2009
- Steiner P, Erhart P, Heske N, Dumoulin CL, von Schulthess GK, Debatin JF: Active biplanar MR tracking for biopsies in humans. AJR Am J Roentgenol 169(3):735–738, 1997
- Zhang Q, Wendt M, Aschoff AJ, Zheng L, Lewin JS, Duerk JL: Active MR guidance of interventional devices with target-navigation. Magn Reson Med 44(1):56–65, 2000
- Guttman MA, Lederman RJ, Sorger JM, McVeigh ER: Real-time volume rendered MRI for interventional guidance. J Cardiovasc Magn Reson 4(4):431–442, 2002
- Guttman MA, Kellman P, Dick AJ, Lederman RJ, McVeigh ER: Real-time accelerated interactive MRI with adaptive TSENSE and UNFOLD. Magn Reson Med 50(2):315–321, 2003
- Navkar NV, Yeniaras E, Shah DJ, Tsekos NV, Deng Z: Generation of 4D access corridors from real-time multislice MRI for guiding transapical aortic valvuloplasties. Med Image Comput Comput Assist Interv 14(Pt 1):251–258, 2011
- Navkar NV, Deng Z, Shah DJ, Tsekos NV: A framework for integrating real-time MRI with robot control: application to simulated transapical cardiac interventions. IEEE Trans Biomed Eng 60(4): 1023–1033, 2013
- Yeniaras E, Navkar NV, Sonmez AE, Shah DJ, Deng Z, Tsekos NV: MR-based real time path planning for cardiac operations with transapical access. Med Image Comput Comput Assist Interv 14(Pt 1):25–32, 2011
- Jolesz FA, Nabavi A, Kikinis R: Integration of interventional MRI with computer-assisted surgery. J Magn Reson Imaging 13(1):69– 77, 2001
- Lewin JS, Nour SG, Duerk JL: Magnetic resonance imageguided biopsy and aspiration. Top Magn Reson Imaging 11(3):173–183, 2000
- Eggers H, Weiss S, Boernert P, Boesiger P: Image-based tracking of optically detunable parallel resonant circuits. Magn Reson Med 49(6):1163–1174, 2003

- Quick HH, Kuehl H, Kaiser G, Hornscheidt D, Mikolajczyk KP, Aker S, Debatin JF, Ladd ME: Interventional MRA using actively visualized catheters, TrueFISP, and real-time image fusion. Magn Reson Med 49(1):129–137, 2003
- Seimenis I, Tsekos NV, Keroglou C, Eracleous E, Pitris C, Christoforou EG: An approach for preoperative planning and performance of MR-guided interventions demonstrated with a manual manipulator in a 1.5T MRI scanner. Cardiovasc Intervent Radiol 35(2):359–367, 2012
- Christoforou E, Akbudak E, Ozcan A, Karanikolas M, Tsekos NV: Performance of interventions with manipulator-driven real-time MR guidance: implementation and initial in vitro tests. Magn Reson Imaging 25(1):69–77, 2007
- Tsekos NV, Ozcan A, Christoforou E: A prototype manipulator for magnetic resonance-guided interventions inside standard cylindrical magnetic resonance imaging scanners. J Biomech Eng 127(6): 972–980, 2005
- Yeniaras E, Navkar NV, Syed MA, Tsekos NV: A computational system for performing robot-assisted cardiac surgeries with MRI guidance. Proceedings of the 15th International Transformative Systems Conference, Society for Design and Process Science, 2010, pp. 1–6
- Rincón-Nigro M, Navkar NV, Tsekos NV, Deng Z: GPUaccelerated interactive visualization and planning of neurosurgical interventions. IEEE Comput Graph Appl 34(1):22–31, 2014
- Zhi-Pei L, Lauterbur PC: Principles of magnetic resonance imaging: a signal processing perspective. Wiley-IEEE Press, 2000
- Suga M, Matsuda T, Komori M, Minato K, Takahashi T: Keyhole method for high-speed human cardiac cine MR imaging. J Magn Reson Imaging 10(5):778–783, 1999
- Wacker FK, Elgort D, Hillenbrand CM, Duerk JL, Lewin JS: The catheter-driven MRI scanner: a new approach to intravascular catheter tracking and imaging-parameter adjustment for interventional MRI. AJR Am J Roentgenol 183(2):391–395, 2004
- Tsekos NV, Khanicheh A, Christoforou E, Mavroidis C: Magnetic resonance-compatible robotic and mechatronics systems for imageguided interventions and rehabilitation: a review study. Annu Rev Biomed Eng 9:351–387, 2007
- Guttman MA, McVeigh ER: Techniques for fast stereoscopic MRI. Magn Reson Med 46(2):317–323, 2001
- Navkar N, Yeniaras E, Shah DJ, Tsekos NV, Deng Z: Extracting geometric features of aortic-valve annulus motion from dynamic cardiac mri for guiding interventions. IEEE International Symposium on Biomedical Imaging (ISBI):1302–1305, 2011
- Gao X, Navkar NV, Shah DJ, Tsekos NV, Deng Z: Intraoperative registration of preoperative 4D cardiac anatomy with real-time MR images. 2012 IEEE 12th International Conference on Bioinformatics & Bioengineering (BIBE), 2012, pp. 583–588
- Yeniaras E, Lamaury J, Navkar NV, Shah DJ, Chin K, Deng Z, Tsekos NV: Magnetic resonance based control of a robotic manipulator for interventions in the beating heart. 2011 IEEE International Conference on Robotics and Automation, 2011, pp. 6270–6275
- Navkar NV, Deng Z, Shah DJ, Bekris K, Tsekos NV: Visual and force-feedback guidance for robot-assisted interventions in the beating heart with real-time MRI. IEEE International Conference on Robotics and Automation (ICRA) 2012, St Paul, MN, 2012, pp. 689–694.
- 34. Bernstein M, King K, Zhou X: Handbook of MRI pulse sequences, 1st edition. Chapter 10.1, Elsevier Academic Press, 2004, p. 292
- Kettenbach J, Wong T, Kacher D, Hata N, Schwartz RB, Black PM, Kikinis R, Jolesz FA: Computer-based imaging and interventional MRI: applications for neurosurgery. Comput Med Imaging Graph 23(5):245–258, 1999
- Gering DT, Nabavi A, Kikinis R, Hata N, O'Donnell LJ, Grimson WE, Jolesz FA, Black PM, Wells WM: An integrated visualization



- system for surgical planning and guidance using image fusion and an open MR. J Magn Reson Imaging 13(6):967-975, 2001
- Nguyen TD, Ding G, Watts R, Wang Y: Optimization of view ordering for motion artifact suppression. Magn Reson Imaging 19(7):951–957, 2001
- Jhooti P, Keegan J, Gatehouse PD, Collins S, Rowe A, Taylor AM, Firmin DN: 3D coronary artery imaging with phase reordering for improved scan efficiency. Magn Reson Med 41(3):555–562, 1999
- 39. Morales Mojica CM, Navkar NV, Tsekos NV, Tsagkaris D, Webb A, Birbilis T, Seimenis I: Holographic Interface for three-dimensional visualization of MRI on HoloLens: a prototype platform for MRI guided neurosurgeries. IEEE 17th International Conference on Bioinformatics and Bioengineering (BIBE), 2017, pp. 21–27

